Universiteit Antwerpen

This item is the archived peer-reviewed author-version of:

$LaFeO_3$ nanofibers for high detection of sulfur-containing gases

uantwerpen.be

LaFeO Nanofibers for High Detection of Sulfur-containing Gases

Albert Queraltó, David Graf, Robert Frohnhoven, Thomas Fischer,
Hans Vanrompay, Sara Bals, Ausrine Bartasyte, and Sanjay Mathur

Just Accepted

LaFeO$_3$ Nanofibers for High Detection of Sulfur-containing Gases

Albert Queraltó,[†,,1] David Graf,[†,1] Robert Frohnhoven,[1] Thomas Fischer,[1] Hans Vanrompay,[2] Sara Bals[2], Ausrine Bartasyte[3] and Sanjay Mathur*[,1]*

[1]Institute of Inorganic Chemistry, University of Cologne, Greinstraße 6, 50939 Cologne, Germany.

[2]Electron Microscopy for Materials Science (EMAT), University of Antwerp, Campus Groenenborger, Groenenborgerlaan 171, 2020 Antwerpen.

[3]FEMTO-ST Institute, University Franche-Comte, 26 rue de l'Epitaphe, 25030 Besancon, France.

†The authors contributed equally to this work.
*Corresponding Authors:

Dr. Albert Queraltó

E-mail: albert.queralto.lopez@gmail.com

Tel. **+49 221 470 3070**

Prof. Dr. Sanjay Mathur

Tel. +49 221 470 4107

E-mail: sanjay.mathur@uni-koeln.de

ABSTRACT

Lanthanum ferrite nanofibers were electrospun from a chemical sol and calcined at 600 ºC to obtain single-phase LaFeO$_3$ (LFO) perovskite. High-resolution transmission electron microscopy in conjunction with 3D tomographic analysis confirmed an interwoven network of hollow and porous (surface) LFO nanofibers. Owing to their high surface area and p-type behavior, the nanofiber meshes showed high chemoselectivity towards reducing, toxic gases (SO$_2$, H$_2$S) that could be reproducibly detected at very low concentrations (<1 ppm) well below the threshold values for occupational safety and health. An increased sensitivity was observed in the temperature range 150-300 ºC with maximum sensor response at 250 ºC. The surface reaction at the heterogeneous solid (LFO) / gas (SO$_2$) interface was investigated

by X-ray photoelectron spectroscopy that confirmed the formation of $La_2(SO_4)_3$. Moreover, the LFO fibers showed a high selectivity in the detection of oxidizing and reducing gases. Whereas superior detection of NH_3 and H_2S was measured, little response was observed for CO and NO_2. Finally, the integration of nanowire meshes in commercial sensor platforms was successfully demonstrated.

KEYWORDS (6 max): $LaFeO_3$, nanofibers, SO_2, H_2S (sulfur-containing gases), electrospinning, chemoresistive gas sensors.

INTRODUCTION

Development of reliable gas sensing devices with enhanced detection capabilities is vital for applications such as environmental monitoring, food inspection and medical diagnostics [1-3]. Particularly challenging is the detection of hazardous gases such as SO_2 and H_2S, which originate from geothermal activity, as well as from anthropogenic origin such as the combustion of fossil fuels in power plants or from smelting factories [4-6]. The serious threat to human life (e.g., acute respiratory issues, nervous system disorders, etc.) and vegetation (e.g., acidic rain) that these gases pose in very small amounts, in the range of ppb and low ppm, have led to strict control measures by regulatory bodies [7-9]. Hence, the need of chemospecific and highly sensitive sensors is needed to address such issues. **Table 1** shows a list of the permissible exposure limits (PELs) of the most generally known gases resulting from the combustion of fossil fuels.

Table 1. Permissible Exposure Limits (PELs) of common toxic gases derived from the combustion of fossil fuels, published by the Occupational Safety and Health Administration [10].

Gas	Permissible Exposure Limits (PELs) in ppm
Sulfur dioxide, SO_2	5
Dihydrogen sulfide, H_2S	20

Ammonia, NH_3	50
Carbon monoxide, CO	50
Carbon dioxide, CO_2	5000
Nitrogen monoxide, NO	25
Nitrogen dioxide, NO_2	5

Semiconductor monometal oxides have been explored for their use in chemoresistive gas sensors due to their change in resistance upon adsorption or desorption of analyte molecules that create a space charge zone, showing high detection capabilities [11-15]. Perovskite oxides (ABO_3) have been identified as promising sensor materials due to their interesting properties such as high electrical conductivity, ferro- and piezoelectricity, multiferroicity, and catalytic activity for surface-driven reduction/oxidation reactions [16-20]. In addition, the multimetal structure of perovskites enables a higher degree of tunability of these properties due to the overlap between filled O^{2-} p-orbitals and unfilled orbitals of the metal cations when compared to their monometal counterparts. Although $LaFeO_3$ (LFO) is a well-known p-type semiconductor, only few works have investigated its sensing capabilities, showing response in the presence of relatively large amounts of gases such as ethanol, CO and NO_2, i.e., gas quantities of 200 ppm and larger [21, 22]. The general sensing behavior of p-type semiconducting oxides is caused by the adsorption, dissociation and ionization of oxygen species (O^- and O^{2-}) on the surface of the material [23]. In air ambient, oxygen species are formed leading to a large accumulation holes in the valence band that acts as conduction channel for electrons [24]. Upon reaction with a reducing gas such as SO_2 or H_2S, the ionosorbed oxygen will combine with the gas molecules and electrons will be injected back into the material, recombining with the holes in the valence band and leading to an increase in the resistance (**Figure 1**). The influence of the grain size in gas

sensing also differs depending on the type of semiconductor [25, 26]. In p-type semiconductors, the hole-accumulation layers located at the grain boundaries act as charge-carrier transport pathways between grains. This means that hole transport through grains is not hindered since no potential barriers exist (**Figure 1**). Therefore, the influence of grain growth on p-type sensing has a much less significant effect compared to the n-type counterpart, as reported previously by Choi and coworkers [26].
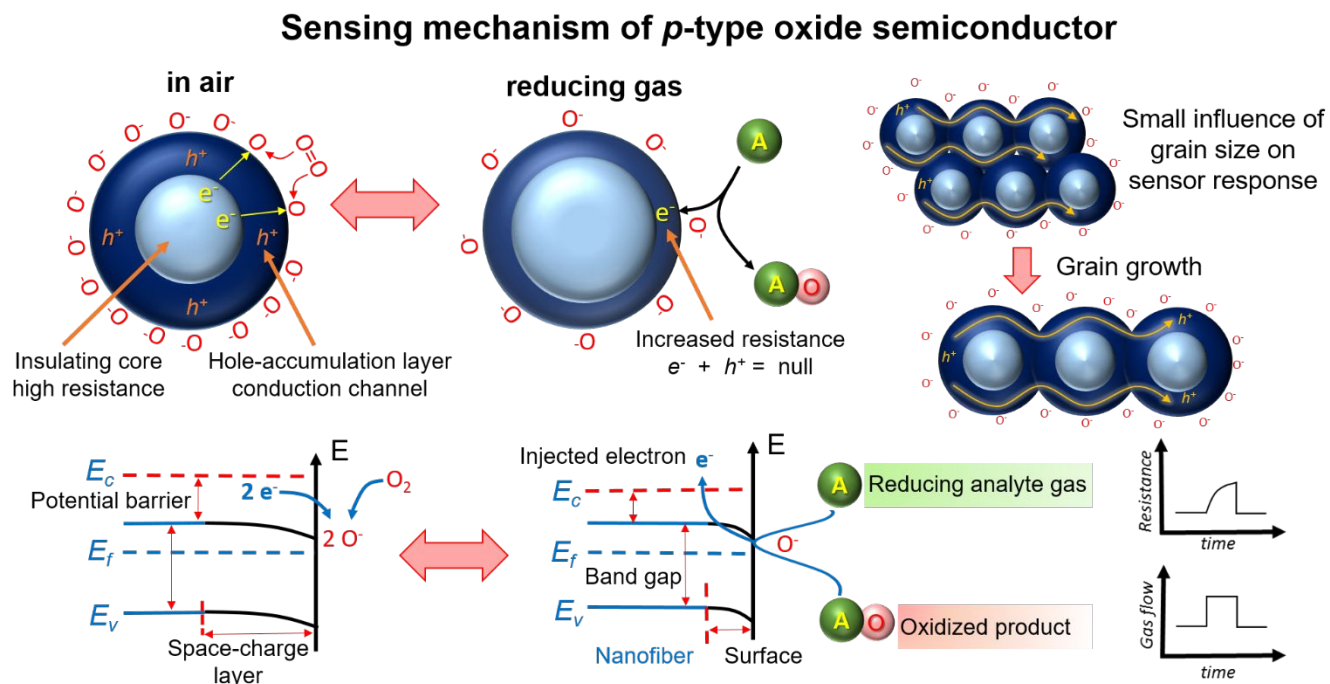

Figure 1. *Schematic representation of the detection mechanism for p-type semiconducting oxides towards reducing analyte gases, as well as the general conduction mechanism between grains.*

The smart engineering of novel and complex architectures through strategies such as patterning [27-29], surface modification [30] and nanostructuration [19, 20, 31] have been explored aiming

for higher device performances, as well as the low-cost and large-scale manufacturing of gas sensing devices. One-dimensional (1D) oxide nanostructures are highly suitable for the integration of active gas sensing materials due to their superior charge transport, high specific surface area, miniaturization and detection capabilities [32-41]. The search for cost-effective, high-throughput nanostructuring strategies has driven the research towards electrospinning. The inherent advantages of metal oxide nanofiber networks such as high porosity, large surface areas, size confinement and interconnectivity have led to significant improvements in device performances for different applications (e.g., Li-ion batteries, photovoltaics, photocatalysis, etc.) [42-50], as well as the fabrication of gas sensing devices with enhanced response and recovery rates [1, 51-54].

In this work, we investigated the sensing capabilities of LFO nanofibers as a function of the temperature and concentration of reducing gases. The focus is on the detection of very low concentrations of toxic sulfur-containing gases such as SO_2 and H_2S. In addition, a comparison with other gases was made to confirm the selectivity of the fabricated sensors. The interdependence between structure, porosity of the nanofiber networks and surface reaction mechanism were evaluated in detail to achieve a high-detection performance.

MATERIALS AND METHODS

Synthesis of LaFeO$_3$ nanofibers

LaFeO$_3$ (LFO) nanofibers were synthesized by electrospinning. The precursor solution with a 0.2 M concentration was prepared by the following procedure. $La(NO_3)_3 \cdot 6H_2O$ and $Fe(NO_3)_3 \cdot 9H_2O$ precursor

salts (Sigma Aldrich) were dissolved in an ethanol/acetic acid solution (6:4 ratio). Then, polyvinylpyrrolidone (PVP, Mw = 1 300 000 g mol^{-1}, Sigma Aldrich), in a proportion of 0.075 g ml^{-1}, was slowly added to the metal nitrate solutions while continuously stirring to obtain a viscous solution. The precursor solution was then transferred into 5 ml plastic syringes and electrospun with a micro-infusion pump at a rate of 10 µl min^{-1}, a high voltage of 10-15 kV and a distance between the tip of the syringe nozzle and the collector of 10 cm. The as-spun nanofibers were calcined at 500 ºC and 600 ºC for 5 h at a heating rate of 1 ºC min^{-1} in air to obtain the crystalline perovskite phase.

Characterization of the nanofibers

The phase characterization of the nanofibers was performed by X-ray diffraction (XRD) with a STOE STADI MP diffractometer equipped with a Mo source (λ=0.7107 Å). Overnight measurements were performed in order to decrease the signal-to-noise ratio by performing steps of 0.02º and integrating over multiple scans. The morphological characterization of the samples was performed by scanning electron microscopy (SEM) using a QUANTA FEI 200 FEG-ESEM.

HAADF-STEM images were acquired using Tecnai Osiris microscope operated at 200 kV. For electron tomography, the samples were mounted on a Fischione tomography holder (model 2020) and tilted over an angular range of ±74° with a 3° increment. After the acquisition, the images were aligned with respect to each other using a phase correlation procedure [55-58]. The outcome was used as an input for the ASTRA toolbox implementation of the Expectation-Maximization algorithm (EM) [59, 60].

High-resolution transmission electron microscopy (HRTEM) was performed with a JEOL JEM-2200FS 200 kV FEG TEM with in-column filter and UHR pole piece. Experimental selective area electron diffraction (SAED) patterns were fitted with CrysTBox software by M. Klinger [61], using the CIF file for LaFeO$_3$ (ICSD-29234).

X-ray photoelectron spectroscopy (XPS) measurements were performed at a pressure in the 10^{-9} mbar range, using an ESCA M-Probe Spectrometer from Surface Science Instruments, equipped with a monochromatic Al Kα excitation source (λ=8.33 Å). Survey scans were acquired with a detector pass energy of 158.9 eV, whereas high-resolution spectra were recorded with a pass energy of 22.9 eV. Binding energies for all spectra were charge-corrected in reference to the C 1s signal for adventitious carbon (284.8 eV). Deconvoluted peaks in the high-resolution spectra were fitted with GL(30) line shapes and a Shirley type background. Spectral corrections and peak deconvolution were done with CasaXPS software (Casa Software Ltd.).

Sensor fabrication and gas sensing measurements

The sensor experiments were carried out with a customized gas sensing system consisting of electronic mass-flow controllers, sensor chamber, sensor chip and Keithley sourcemeters for heating and measuring the electrical resistance of the nanofibers. The gas sensing station was controlled using the LabView software (National Instruments), and the heating element was calibrated before the gas sensing experiment. The atmosphere composition was preassigned by means of electronic mass-flow controllers (Aera FC-7700C), mixing flows coming from certified bottles (Air Products and Chemicals, Inc.) containing a given amount of the target gas (SO_2, H_2S, NH_3, CO and NO_2) and diluted in synthetic air with the background flow. The background atmosphere was generated from a dry air bottle (Air Products and Chemicals, Inc.) certified for no humidity that ruled out any surface reactions with moisture.

Since the nanofibers were calcined at 600 ºC and the temperatures used during the sensing experiments were well below (150 to 300 ºC), no thermally-induced changes were expected in the materials.

The sensitivity S was determined by the formula (Equation 1):

$$S\ (\%) = \frac{R_g - R_a}{R_a} \times 100,\qquad\qquad (1)$$

where R_a and R_g are the resistance in the presence of synthetic air and target gas, respectively. The response and recovery times have been defined as the time required to reach a 90% variation in the resistance upon the introduction or removal of the target gas.

RESULTS AND DISCUSSION

Electrospun nanofibers are beneficial as active materials for gas sensing devices because the large space-to-volume ratio and porous structure of nanofiber meshes can be coupled with their excellent surface activities [51]. In addition, the directional charge-carrier transfer and enhanced pathways created by nanofibers as compared to conventional grain boundaries [25, 26], promote charge carrier circulation, which could eventually improve the sensing capabilities, as well as the response and recovery times of gas sensors.

Structural and morphological characterization

The as-spun LaFeO$_x$/PVP nanofibers were calcined at temperatures of 500 and 600 ºC for 5 h with a heating ramp of 1 ºC min^{-1} [22, 50]. X-ray diffraction (XRD) patterns of the nanofibers were collected after calcination at 500 ºC and 600 ºC (Figure 2a). The sample calcined at 500 ºC shows a broad peak ranging from 10º to 15º, which indicates the amorphous/nanocrystalline state of the nanofibers. Some insipient peaks, which could be barely distinguished from the noise, are likely attributed to the final LaFeO$_3$ (LFO) phase, as well as other lanthanum and iron containing phases. The LFO perovskite phase is formed after calcination at 600 ºC. A *Pm-3m* spacegroup with a pseudocubic theoretical lattice parameter a=3.926 Å has been used to fit the diffraction pattern (ICSD-29234). An average crystallite size of approximately 58.1±14.7 nm is estimated after fitting of the (110) peak located at 14.68º using the Debye-Scherrer formula [62].

SEM shows that continuous fiber mats of LaFeO$_x$/PVP obtained after electrospinning exhibit a smooth surface, uniform widths with average diameters of 360±150 nm and lengths in the micrometer-to-

millimeter range (Figure 2b). After calcination at 600 ºC (Figure 2c), LFO nanofibers possess average diameters about 50-60% smaller (200±90 nm), when compared to as-spun nanofibers, due to the decomposition of the PVP during the calcination process. Their length is also shrunk in some areas due to brittleness after the polymer is removed from their structure during calcination. The surface of the nanofibers becomes porous, granular and rougher with grains ranging from approximately 50 to 100 nm, rather similar sizes compared to the average crystallite values obtained by XRD.

1
2
3
4
5
6
7
8
9
10
11
12
13
14
15
16
17
18
19
20
21
22
23
24
25
26
27
28
29
30
31
32
33
34
35
36
37
38
39
40
41
42
43
44
45
46
47
48
49
50
51
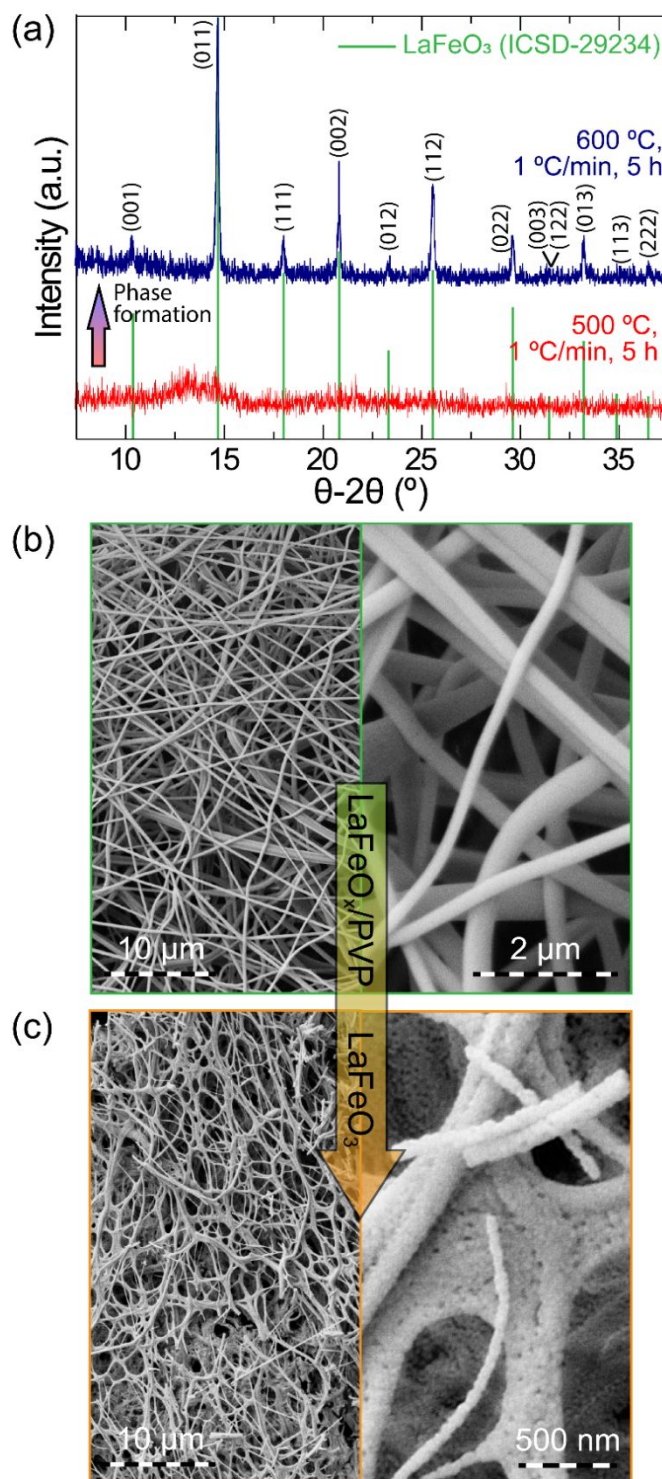52
53
54
55
56
57
58
59
60

Figure 2. *(a) Indexed XRD patterns of LFO (ICSD-29234) nanofibers annealed at 500 and 600 ℃ for 5 h with a heating ramp of 1 ℃ min⁻¹ in air. SEM micrographs depicting the intertwined morphology of the as-spun (a) LaFeOₓ/PVP nanofibers after electrospinning, as well as (b) LFO nanofibers after calcination at 600 ℃ for 5 h with a heating ramp of 1 ℃ min⁻¹ in air.*

HAADF-STEM and HRTEM characterizations allow a closer look on the morphology of the nanofibers (Figure 3a – 3c). The LFO nanofibers consist of smaller units connected between each other (Figure 3a). HRTEM measurements reveals a structure with different contrasts, resembling a shell (Figure 3c). Their diameters have values around 60-80 nm, which agrees quite well with the previously estimated dimensions via XRD and SEM. The SAED pattern depicts the experimental polycrystalline rings of the LFO nanofibers, as well as a peak view of the ring intensities (Figure 3d). The ring intensities were correlated with the (001), (011), (111), (002) and (112) reflections, having interplanar spacing values of 3.926, 2.776, 2.267, 1.963 and 1.603 Å, as well as theoretical intensities larger than 20 %. The (012) reflection, depicted as a red line in the peak view, is not present in the experimental measurements due to its low intensity of <6 %. This is also in agreement with the intensity of the XRD peaks (Figure 2a). An experimental lattice parameter a=3.92 Å was calculated by fitting of the experimental rings. This value differs approximately 0.15 % with respect to the theoretical lattice parameter (3.926 Å). This small difference in the values could be either caused by instrumental error, as well as other phenomena such as the presence of anion or cation vacancies, nanoscale size and shape effects, as well as nanostrain which are known to highly influence the lattice parameters [19, 63-67]. Electron tomography was employed in order to better understand the 3D morphology of the nanofibers and validate if the structure was indeed porous or not (Figure 3e). The direction of the slices is indicated in the right-top corner (Figure 3f). From the orthoslices through the 3D reconstruction, we see in fact that the nanofibers' structure is in fact porous and hollow, confirming our previous speculations, also containing several interconnections between the exterior shell.
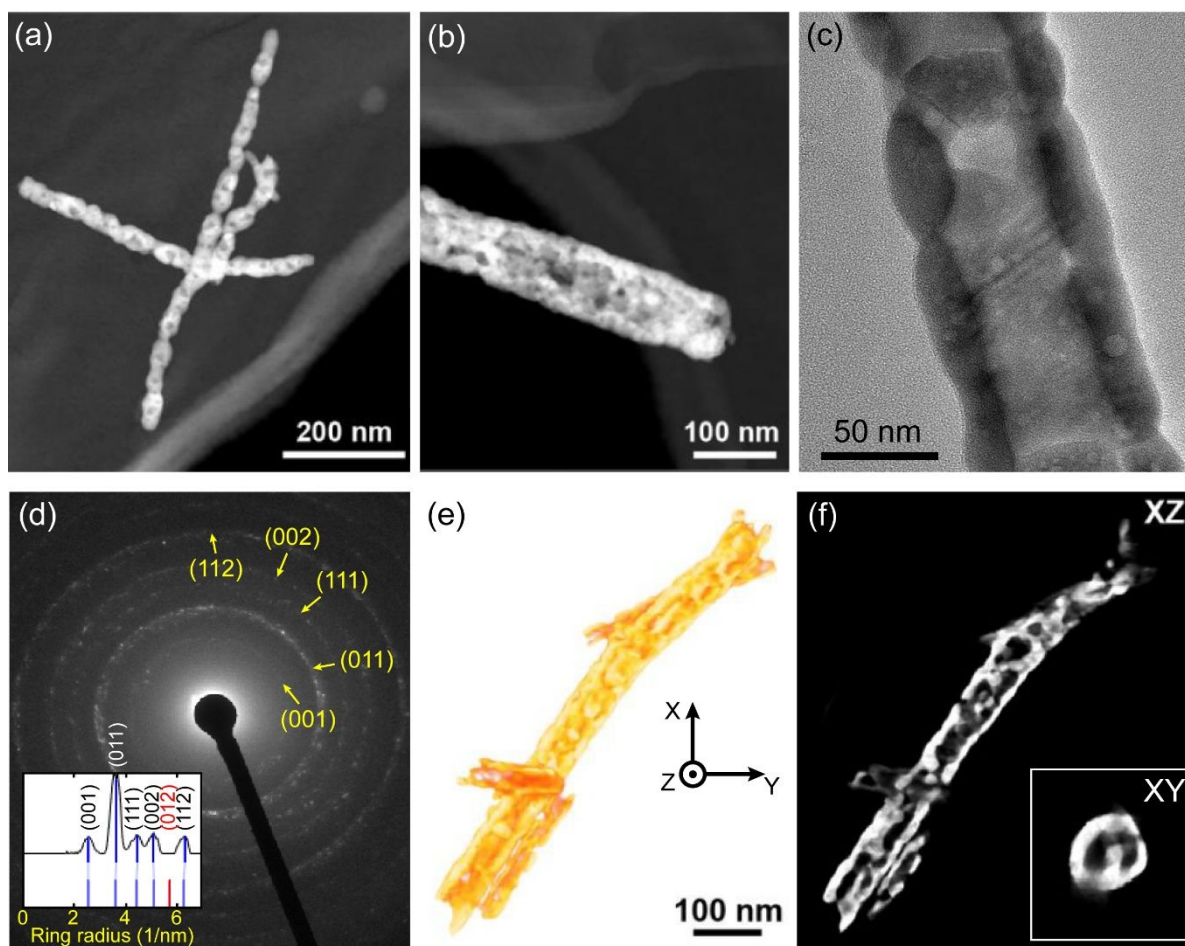
Figure 3. *(a,b) HAADF-STEM and (c) HRTEM characterization of the LFO nanofibers. (d) SAED pattern of (c), depicting the experimental polycrystalline rings, as well as the peak view of the ring intensities (inset) obtained from fitting the experimental data with the CrysTBox software by M. Klinger [61], using the CIF file for LaFeO₃ (ICSD-29234). (e) 3D rendering of the LFO nanofibers morphology, (f) orthogonal slice in the XZ axis, revealing the interior of the structure. Inset: Slice along the XY axis, depicting the hollow structure of the nanofiber.*

Gas sensing properties and surface chemistry

The gas-solid interactions of the obtained porous LFO nanofiber network were investigated in presence of different reducing gas molecules. LFO exhibits p-type semiconducting

characteristics and, therefore, the electrical resistance upon exposure to the reducing gas

(Figure 1) is expected to increase [24, 68, 69].

The sensor response to SO_2 revealed a very high detection capability of the manufactured

sensor at very low concentrations from 0.5 to 4 ppm and a temperature range from 150 to 300

ºC (Figure 4). The intrinsic nature of SO_2 allows it to act as reducing as well as oxidizing

molecule, depending on the material surface and operating temperature [70-73]. The resistance

of porous LFO nanofiber-based sensors increased significantly after the introduction of SO_2

(Figure 4a). Hence, SO_2 interacts with the ionosorbed oxygen species, followed by its oxidation

to SO_3 which is accompanied by the donation of electrons into the conduction band (Equation

2).

$$SO_2(gas) + O^-(ads) \longrightarrow SO_3 + e^- \tag{2}$$

A significant response towards very low concentrations of SO_2 down to 0.5 ppm which is ten

times lower than the threshold limit values published by the Occupational Safety and Health

Administration (OSHA) was observed [10]. As the temperature rose, the sensitivity initially

increased and subsequently decreased with the optimum working temperature at 250°C. This

behavior results from the increasingly higher amount and mobility of receptor species (O^- and

O^{2-}) on the nanofibers' surface and the faster kinetics of the gas-solid reactions with

temperature. At 300°C, the desorption of SO_2 molecules is high enough to dominate the process

and, hence, the sensitivity decreases. The calculated response times were between 90 and 240

s, while the recovery times were estimated to lie between 300 and 500 s, depending on the

operating temperature. The drift of the initial background resistance increased independently of

the temperature, although this gain seemed to be less pronounced at higher temperatures. As

a result, we calculated the sensitivity and response times for each SO_2 pulse separately by using

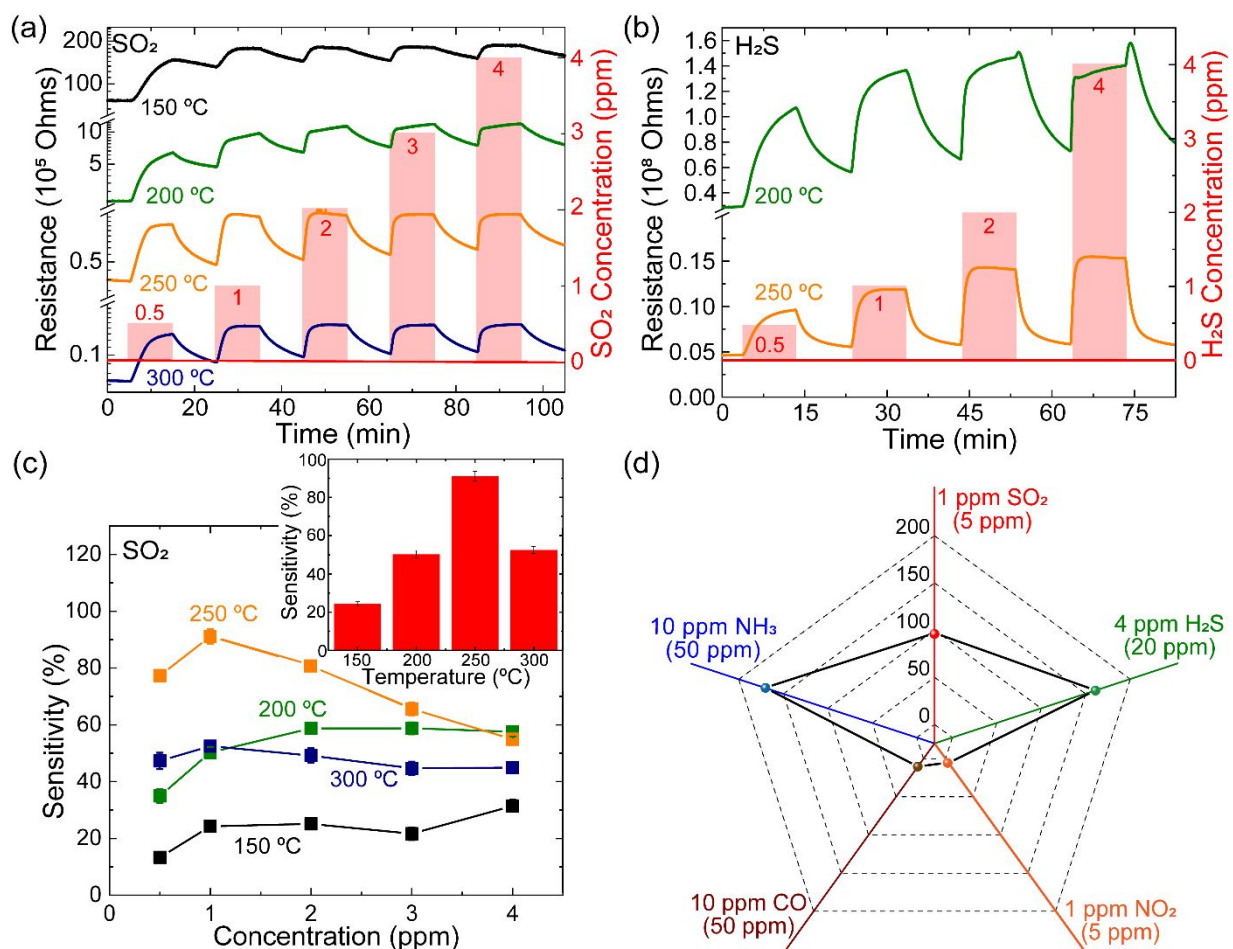the resistance immediately before the SO_2 pulse.

Figure 4. Resistance for LFO nanofiber-based gas sensors for (a) SO_2 and (b) H_2S, measured at concentrations ranging from 0.5 to 4 ppm and temperatures from 150 ℃ 300 ℃. The resistance scale has been divided for better display of the results. (c) Change of the sensitivity as a function of the concentration of SO_2. Insets: Sensitivity dependence on the sensing temperature with a gas concentration of 1 ppm. (d) Sensor sensitivity for 1 ppm SO_2, 4 ppm H_2S, 1 ppm NO_2, 10 ppm NH_3 and 10 ppm CO measured at 250°C. Values five times lower than the PELs (between parenthesis) published by the Occupational Safety and Health Administration (OSHA) have been selected for comparison [10].

Possible reasons for the baseline drift of the sensors could result from structural changes such as sintering effects of the nanofiber network or chemical reactions on the surface [74]. The drift reduction at higher temperatures rather indicates a chemical origin and can be attributed to the temperature dependent adsorption/desorption dynamic equilibria of the SO_2 molecules and the formed sulfite (SO_3^{2-}) or oxidized sulfate (SO_4^{2-}) species on the surface. The strong binding tendency of the sulfur oxide species on the porous LFO surface leads to poisoning of the sensor, which can be reversed at higher temperature due to the accelerated desorption process. Table 2 shows a comparison of different materials used for sensing of S-containing gases and their properties.

Table 2. Comparison of semiconductor oxides for the detection of SO_2 and H_2S.

Sensor material	Morphology	Measured ppm range	Operating Temperature range (°C)	Sensitivity (%)	Response (s) / Recovery (s)	Ref.
SO₂ gas sensors						
SnO_2/TiO_2	Powder	10-40	400-500	70 (450 °C, 40 ppm)	300 / 600	[75]
SnO_2	Nanoparticles	5 and 100	250-450	20 (350 °C, 5 ppm)	-	[71]
0.15 wt% V_2O_5:SnO_2				45 (350 °C, 5 ppm)		
Au:SnO_2		0.5-20	200	75 (200 °C, 20 ppm)	34-60 / 14-31	[76]
PdO:SnO_2	Film and nanoclusters	500	100-300	12 (200 °C)	170 / 100	[77, 78]
CuO:SnO_2				5 (160 °C)	200 / 150	
NiO:SnO_2				56 (180 °C)	80 / 70	
MgO:SnO_2				2 (120 °C)	125 / 120	
V_2O_5:SnO_2				1.5 (240 °C)	106 / 115	
WO_3	Powder	200-800	100-800	12 (400 °C, 800 ppm)	-	[79]
1.0 wt% Ag:WO_3				20 (450 °C, 800 ppm)		
WO_3	Film	1-10	200-300	<2 (260 °C, 10 ppm)	-	[80]
Ru/Al_2O_3/ZnO	Nanosheets / microspheres	25-115	250-500	65 (350 °C, 25 ppm)	60 / 360 (at 5 ppm)	[81]
$BiFeO_3$	Nanoparticles	5	300	85	20 / 50	[72]
$LaFeO_3$	Nanofibers	0.5-4	150-300	20-90	90-240 / 300-500	This work
H₂S gas sensors						
ZnO	Nanowires	0.05-1	300	53 (at 1 ppm)	1800 / 2000 (at 1 ppm)	[33]
SnO_2/rGO	Nanocomposite	50	22	33	2 / 292	[82]
$LaFeO_3$	Nanofibers	0.5-4	200 and 250	160 (250 °C and 4 ppm)	60-360 / 180-500	This work

In order to explain the sensing mechanism, the surface composition of LFO nanofibers was investigated by XPS analyses before and after SO_2 (4 ppm) treatment at 250 °C without a recovery step in synthetic air. Both survey spectra (**Figure 5a** and **S1a**) reveal the typical signals for lanthanum, iron, oxygen and carbon while the Fe:La ratio can be estimated to be close to 1:1 (**Table S1**). The survey spectrum of SO_2-treated LFO (**Figure 5a**) clearly reveals sulfur peaks (S 2p at ~160-169 eV, 2s at ~230 eV). The high-resolution spectra for C 1s, O 1s and the La 3d (**Figure S1**) of the untreated LFO state a high degree of lanthanum carbonate formation on the sample surface due to the reaction of LFO with ambient CO_2 [83].

In the deconvoluted La 3d spectrum, the contribution of lanthanum carbonates is determined to be 77.55 at%, whereas 22.45 at% are contributed from LFO. Going along with the degradation of LFO during carbonate formation, the Fe 2p spectrum shows 28.89 at% of Fe^{2+} bond to oxygen (main peaks at 708.30 eV, 709.60 eV, 710.80 eV, and 712.00 eV) as well as 71.11 at% of Fe^{3+} (709.60 eV, 710.60 eV, 711.40 eV, 712.50 eV, and 713.50 eV) from LFO (and most probably also Fe_2O_3 - expected multiplet binding energies of Fe_2O_3 and LFO are in the same range). The mixed valence of iron is also expressed by the fact that no clear satellite peak neither for Fe^{3+} (~719.3 eV) nor Fe^{2+} (~715.4 eV) can be resolved.

The treatment with reducing and corrosive SO_2 gas leads to changes in the surface composition as the presence of sulfur in the survey spectrum already implicates. The S 2p high-resolution spectrum (**Figure 5b**) discloses the formation of sulfate species during the SO_2 treatment of LFO nanofibers with components at 168.78 eV (S $2p_{3/2}$) and 169.96 eV (S $2p_{1/2}$). The high-resolution spectra of the La 3d region (**Figure 5c**) and the Fe 2p region (**Figure 5d**) of the SO_2-treated sample suggest the formation of $La_2(SO_4)_3$, since there is no remarkable shift to higher binding energies in the Fe 2p peak indicating a formation of iron sulfate [84], whereas the La $3d_{5/2}$ peak needs a third deconvoluted duplet for $La_2(SO_4)_3$ at higher binding energies (836.11 eV and 838.71 eV) than LFO (834.01 eV and 838.61 eV) and $La_2(CO_3)_3$ (834.51 eV and 837.91 eV). The formation and surface poisoning of $La_2(SO_4)_3$ during exposition to SO_2 has previously been reported by Zhu et al. for $LaCoO_3$, going along with the formation of CoO [85]. The formation of $La_2(SO_4)_3$ instead of $Fe_2(SO_4)_3$ or $FeSO_4$ could be promoted due to the ability of lanthanum cations to adopt higher coordination numbers (CN > 6) and softer acidity due to the larger ionic radii, increasing its bonding probability with SO_4^{2-}. The proposed reaction mechanism of SO_2 to sulfate species and desorbed SO_3 is illustrated in **Figure 6**. The poisoning effects on the sensor cannot be completely exclude at lower temperature due to the strong binding energy and slow desorption kinetics of the sulfate species. Notably, the portion of $La_2(CO_3)_3$ decreases from 77.55 at% in the sample before sensing to 28.59 at% after SO_2 gas sensing, while the amount of LFO increases to 44.87 at% at the same time; the contribution from $La_2(SO_4)_3$ to the La 3d peak is 26.54 at%. Along with this, the amount of Fe^{2+}

in the Fe 2p signal is reduced to 12.97 at% and the amount of Fe^{3+} raises to 87.03 at%. These observations indicate corrosive etching of the sample surface during gas sensing with SO_2; the decrease of the lanthanum carbonate layer allows the X-rays to penetrate deeper into the bulk material.
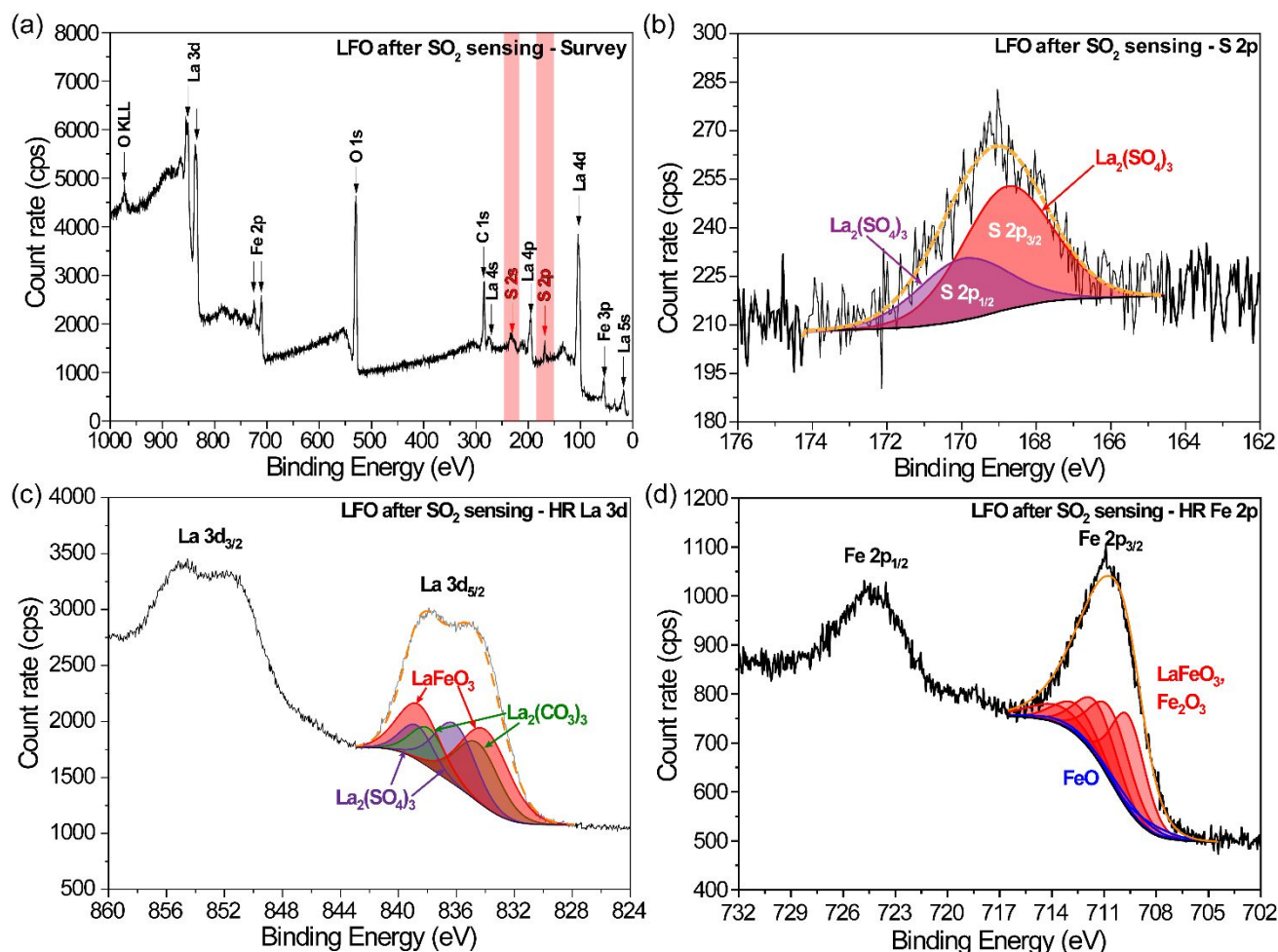

Figure 5. XPS spectra for LFO nanofibers after SO_2 sensing: (a) survey, and high-resolution (b) La 3d region, (c) S 2p region and (d) Fe 2p region.
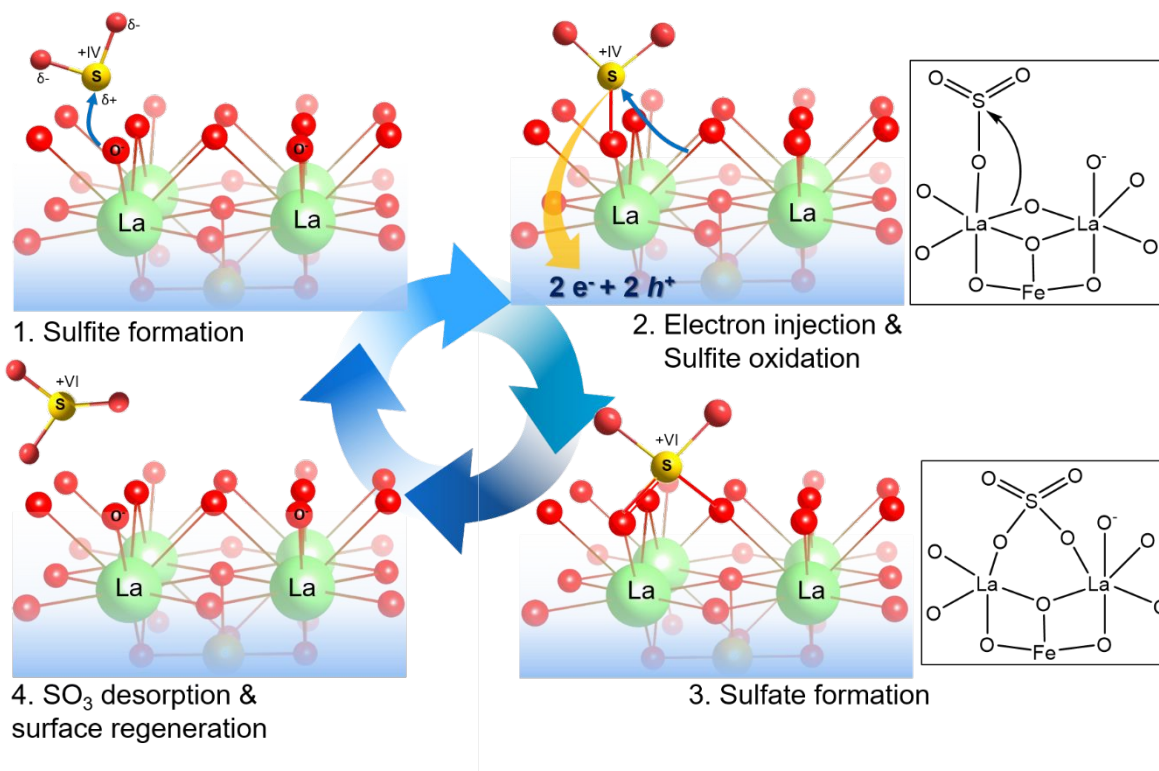
Figure 6. Proposed reaction mechanism of SO_2 to sulfate species with LFO nanofibers and the desorbed SO_3.

The performance of the LFO-based sensor decreased under 20% humidity and displayed an increase of the initial baseline resistance, as well as a high signal-to-noise ratio (**Figure S4**). At higher humidity levels, SO_2 molecules could not be detected precisely. The change in sensitivity resulted possibly due to the formation of hydroxyl groups on the surface and gas phase reaction of SO_2 with water molecules to sulfurous acid (H_2SO_3) or to the more thermodynamically stable bisulfite ion (HSO_3^-). For improved detection capabilities under humid conditions, filtering elements such as zeolites should be integrated in the sensor architecture [86].

In addition, the sensitivity of the fabricated porous LFO nanofiber network towards other toxic

gases was investigated (Figure S2) by using five times lower concentrations than the permissible

exposure limits (PELs) [10]. For reducing gases like NH_3 and H_2S, an increase in the resistance was

observed, as expected. The assumed sensing mechanism is given in equation 3 and 4 [87, 88].

$$2H_2S + O_2^- \longrightarrow 2SO_2 + 2H_2O + 3e^- \tag{3}$$

$$\begin{cases} 2NH_3 + 3O^- \longrightarrow N_2 + 3H_2O + 3e^- \\ \qquad\qquad or \\ 4NH_3 + 3O_2^- \longrightarrow 2N_2 + 6H_2O + 3e^- \end{cases} \tag{4}$$

In the case of H_2S, again a small drift of the initial background resistance was observed at 200 °C, whereas

at 250 °C very stable and sensitive gas response signals (160 %) are found (Figure 4d). A measurement

artifact was measured in the signal at 200 °C for 2 and 4 ppm, which has been attributed to the dilution

procedure with the mass flow controllers. Additionally, the sensitive nature of the hollow LFO fibers

towards reducing corrosive gases was evidenced with the 170% response value for 10 ppm NH_3. Further

investigations of nitrogen-containing gases at lower concentrations would be required to ascertain

accurate sensitivity values. Although this is outside the scope of this article, the gas concentration is

approximately two and ten times larger than the one of H_2S and SO_2, respectively. Thus, one could

estimate that lower sensitivity values will be obtained. Finally, a very low response was detected for 10

ppm CO (non-corrosive, reducing) and 1 ppm NO_2 (corrosive, oxidizing), 10% and 8%, indicating the

high selectivity of the fabricated sensor for low reducing gas concentrations. The stability of the sensor

was confirmed by X-ray diffraction after all gas sensing experiments, which displayed no phase change

of $LaFeO_3$ or other impurities such as $La_2(SO_4)_3$ or iron oxides.

CONCLUSIONS

Direct integration of phase pure $LaFeO_3$ nanofibers on a single sensor chip was achieved by electrospinning approach. Morphological investigations revealed a highly hollow, porous and continuous fiber network which led to superior sensing capabilities of reducing toxic gases SO_2 and H_2S. The sensing of very low concentrations of sulfur-containing gases revealed a high potential for environmental monitoring in regions with geothermal/volcanic activity, as well as air pollution from the combustion of fossil fuels, which is of high public and research interest. The detection limits of H_2S and SO_2 were reduced down to 0.5 ppm by optimizing the working temperature. The analysis of the surface chemistry allowed an in-depth investigation of the SO_2 interaction with the $LaFeO_3$ surface, promoting the formation of SO_4^{2-} and the injection of electrons directly to the conduction band of the p-type semiconductor. We assume that faster recovery and stable background resistance were achieved at higher temperatures due to the desorption of SO_4^{2-} through the formation of SO_3 gas molecules. The low response towards CO and NO_2 shows the good selectivity of the manufactured sensors. We have demonstrated the high detection capabilities of electrospun p-type semiconducting LFO nanofiber-based gas sensors towards reducing gases which is of enormous importance for the environmental monitoring and protection.

Present Address

Dr. Albert Queraltó

Institut de Ciencia de Materials de Barcelona (ICMAB-CSIC)

Campus UAB, 08193 Bellaterra, Catalonia, Spain

Tel. +34 93 580 1853 (ext 382)

Fax. +34 93 580 5729

Supporting Information. Additional XPS measurements, elemental composition, additional gas sensing and XRD measurements.

REFERENCES

1. Ding, B., M. Wang, X. Wang, J. Yu, and G. Sun, *Electrospun nanomaterials for ultrasensitive sensors.* Mater. Today, 2010, **13**(11), 16-27, DOI 10.1016/s1369-7021(10)70200-5.

2. Righettoni, M., A. Amann, and S.E. Pratsinis, *Breath analysis by nanostructured metal oxides as chemo-resistive gas sensors.* Mater. Today, 2015, **18**(3), 163-171, DOI 10.1016/j.mattod.2014.08.017.

3. Konstantynovski, K., G. Njio, F. Börner, A. Lepcha, T. Fischer, G. Holl, and S. Mathur, *Bulk detection of explosives and development of customized metal oxide semiconductor gas sensors for the identification of energetic materials.* Sens. Actuators B, 2018, **258**, 1252-1266, DOI 10.1016/j.snb.2017.11.116.

4. McLinden, C.A., V. Fioletov, M.W. Shephard, N. Krotkov, C. Li, R.V. Martin, M.D. Moran, and J. Joiner, *Space-based detection of missing sulfur dioxide sources of global air pollution.* Nat. Geosci., 2016, **9**(7), 496-500, DOI 10.1038/ngeo2724.

5. Carn, S.A., L. Clarisse, and A.J. Prata, *Multi-decadal satellite measurements of global volcanic degassing.* J. Volcanol. Geotherm. Res., 2016, **311**, 99-134, DOI 10.1016/j.jvolgeores.2016.01.002.

6. Bari, M.A., R.L.T. Curran, and W.B. Kindzierski, *Field performance evaluation of Maxxam passive samplers for regional monitoring of ambient SO_2, NO_2 and O_3 concentrations in Alberta, Canada.* Atmospheric Environ., 2015, **114**, 39-47, DOI 10.1016/j.atmosenv.2015.05.031.

7. Hansell, A. and C. Oppenheimer, *Health hazards from volcanic gases: a systematic literature review.* Arch. Environ. Health, 2004, **59**(12), 628-639, DOI 10.1080/00039890409602947.

8. Carn, S.A., V.E. Fioletov, C.A. McLinden, C. Li, and N.A. Krotkov, *A decade of global volcanic SO_2 emissions measured from space.* Sci. Rep., 2017, **7**, 44095, DOI 10.1038/srep44095.

9. Fioletov, V.E., C.A. McLinden, N. Krotkov, C. Li, J. Joiner, N. Theys, S. Carn, and M.D. Moran, *A global catalogue of large SO_2 sources and emissions derived from the Ozone Monitoring Instrument.* Atmospheric Chem. Phys., 2016, **16**(18), 11497-11519, DOI 10.5194/acp-16-11497-2016.

10. Administration, O.S.H. *Permissible Exposure Limits For Chemical Contaminants.* Available from: https://www.cdc.gov/niosh/docs/2005-149/pdfs/2005-149.pdf.

11. Carpenter, M.A., S. Mathur, and A. Kolmakov, *Metal Oxide Nanomaterials for Chemical Sensors.* 1st ed. Integrated Analytical Systems, ed. R.A. Potyrailo. 2013, New York: Springer. 548, DOI 10.1007/978-1-4614-5395-6.

12. Pan, J., R. Ganesan, H. Shen, and S. Mathur, *Plasma-Modified SnO_2 Nanowires for Enhanced Gas Sensing.* J. Phys. Chem. C, 2010, **114**(18), 8245-8250, DOI 10.1021/jp101072f.

13. Maziarz, W., A. Kusior, and A. Trenczek-Zajac, *Nanostructured TiO₂-based gas sensors with enhanced sensitivity to reducing gases.* Beilstein J. Nanotechnol., 2016, **7**, 1718-1726, DOI 10.3762/bjnano.7.164.

14. Von Hagen, R., M. Sneha, S. Mathur, and B. Derby, *Ink-jet Printing of Hollow SnO₂ Nanospheres for Gas Sensing Applications.* J. Am. Ceram. Soc., 2014, **97**(4), 1035-1040, DOI 10.1111/jace.12832.

15. Mathur, S., R. Ganesan, I. Grobelsek, H. Shen, T. Ruegamer, and S. Barth, *Plasma-Assisted Modulation of Morphology and Composition in Tin Oxide Nanostructures for Sensing Applications.* Adv. Eng. Mater., 2007, **9**(8), 658-663, DOI 10.1002/adem.200700086.

16. Fergus, J.W., *Perovskite oxides for semiconductor-based gas sensors.* Sens. Actuators B, 2007, **123**(2), 1169-1179, DOI 10.1016/j.snb.2006.10.051.

17. Catalan, G. and J.F. Scott, *Physics and Applications of Bismuth Ferrite.* Adv. Mater., 2009, **21**(24), 2463-2485, DOI 10.1002/adma.200802849.

18. Queraltó, A., A. Pérez del Pino, M. de la Mata, J. Arbiol, M. Tristany, A. Gómez, X. Obradors, and T. Puig, *Growth of ferroelectric Ba₀.₈Sr₀.₂TiO₃ epitaxial films by ultraviolet pulsed laser irradiation of chemical solution derived precursor layers.* Appl. Phys. Lett., 2015, **106**(26), 262903, DOI 10.1063/1.4923376.

19. Queraltó, A., M. de la Mata, J. Arbiol, X. Obradors, and T. Puig, *Disentangling Epitaxial Growth Mechanisms of Solution Derived Functional Oxide Thin Films.* Adv. Mater. Interfaces, 2016, **3**(18), 1600392, DOI 10.1002/admi.201600392.

20. Queraltó, A., A. Perez del Pino, M. de la Mata, J. Arbiol, M. Tristany, X. Obradors, and T. Puig, *Ultrafast Epitaxial Growth of Functional Oxide Thin Films by Pulsed Laser Annealing of Chemical Solutions.* Chem. Mater., 2016, **28**(17), 6136-6145, DOI 10.1021/acs.chemmater.6b01968.

21. Bai, S., B. Shi, L. Ma, P. Yang, Z. Liu, D. Li, and A. Chen, *Synthesis of LaFeO₃ catalytic materials and their sensing properties.* Sci. China Ser. B: Chem., 2009, **52**(12), 2106-2113, DOI 10.1007/s11426-009-0289-3.

22. Fan, H.T., X.J. Xu, X.K. Ma, and T. Zhang, *Preparation of LaFeO₃ nanofibers by electrospinning for gas sensors with fast response and recovery.* Nanotechnol., 2011, **22**(11), 115502, DOI 10.1088/0957-4484/22/11/115502.

23. Shankar, P. and J.B.B. Rayappan, *Gas sensing mechanism of metal oxides: The role of ambient atmosphere, type of semiconductor and gases -A review.* Sci. Lett. J., 2015, **4**, 126, DOI -.

24. Kim, H.-J. and J.-H. Lee, *Highly sensitive and selective gas sensors using p-type oxide semiconductors: Overview.* Sens. Actuators B, 2014, **192,** 607-627, DOI 10.1016/j.snb.2013.11.005.

25. Katoch, A., G.-J. Sun, S.-W. Choi, J.-H. Byun, and S.S. Kim, *Competitive influence of grain size and crystallinity on gas sensing performances of ZnO nanofibers.* Sens. Actuators B, 2013, **185,** 411-416, DOI 10.1016/j.snb.2013.05.030.

26. Choi, J.-M., J.-H. Byun, and S.S. Kim, *Influence of grain size on gas-sensing properties of chemiresistive p-type NiO nanofibers.* Sens. Actuators B, 2016, **227,** 149-156, DOI 10.1016/j.snb.2015.12.014.

27. Pyeon, M., M. Wang, Y. Gönüllü, A. Kaouk, S. Jäckle, S. Christiansen, T. Hwang, K. Moon, and S. Mathur, *Design of multi-layered TiO_2–Fe_2O_3 photoanodes for photoelectrochemical water splitting: patterning effects on photocurrent density.* MRS Comm., 2016, **6**(04), 442-448, DOI 10.1557/mrc.2016.54.

28. Bialuschewski, D., J.S. Hoppius, R. Frohnhoven, M. Deo, Y. Gönüllü, T. Fischer, E.L. Gurevich, and S. Mathur, *Laser-Textured Metal Substrates as Photoanodes for Enhanced PEC Water Splitting Reactions.* Adv. Eng. Mater., 2018, **20**(9), 1800167, DOI 10.1002/adem.201800167.

29. Queraltó, A., Á. Pérez del Pino, S. Ricart, X. Obradors, and T. Puig, *Laser-induced metal organic decomposition for $Ce_{0.9}Zr_{0.1}O_{2-y}$ epitaxial thin film growth.* J. Alloys Compd., 2013, **574,** 246-254, DOI 10.1016/j.jallcom.2013.04.171.

30. Pyeon, M., T.-P. Ruoko, J. Leduc, Y. Gönüllü, M. Deo, N.V. Tkachenko, and S. Mathur, *Critical role and modification of surface states in hematite films for enhancing oxygen evolution activity.* J. Mater. Res., 2018, **33**(04), 455-466, DOI 10.1557/jmr.2017.465.

31. Obradors, X., T. Puig, M. Gibert, A. Queralto, J. Zabaleta, and N. Mestres, *Chemical solution route to self-assembled epitaxial oxide nanostructures.* Chem. Soc. Rev., 2014, **43**(7), 2200-2225, DOI 10.1039/C3CS60365B.

32. Fiz, R., F. Hernandez-Ramirez, T. Fischer, L. Lopez-Conesa, S. Estrade, F. Peiro, and S. Mathur, *Synthesis, Characterization, and Humidity Detection Properties of Nb_2O_5 Nanorods and SnO_2/Nb_2O_5 Heterostructures.* J. Phys. Chem. C, 2013, **117**(19), 10086-10094, DOI 10.1021/jp3121066.

33. Huber, F., S. Riegert, M. Madel, and K. Thonke, *H₂S sensing in the ppb regime with zinc oxide nanowires.* Sens. Actuators B, 2017, **239,** 358-363, DOI 10.1016/j.snb.2016.08.023.

34. Gad, A.E., M.W.G. Hoffmann, F. Hernandez-Ramirez, J.D. Prades, H. Shen, and S. Mathur, *Coaxial p-Si/n-ZnO nanowire heterostructures for energy and sensing applications.* Mater. Chem. Phys., 2012, **135**(2-3), 618-622, DOI 10.1016/j.matchemphys.2012.05.034.

35. Hernandez-Ramirez, F., J.D. Prades, A. Hackner, T. Fischer, G. Mueller, S. Mathur, and J.R. Morante, *Miniaturized ionization gas sensors from single metal oxide nanowires.* Nanoscale, 2011, **3**(2), 630-634, DOI 10.1039/c0nr00528b.

36. Hernandez-Ramirez, F., J.D. Prades, R. Jimenez-Diaz, T. Fischer, A. Romano-Rodriguez, S. Mathur, and J.R. Morante, *On the role of individual metal oxide nanowires in the scaling down of chemical sensors.* Phys. Chem. Chem. Phys., 2009, **11**(33), 7105-7110, DOI 10.1039/b905234h.

37. Giebelhaus, I., E. Varechkina, T. Fischer, M. Rumyantseva, V. Ivanov, A. Gaskov, J.R. Morante, J. Arbiol, W. Tyrra, and S. Mathur, *One-dimensional CuO–SnO₂ p–n heterojunctions for enhanced detection of H₂S.* J. Mater. Chem. A, 2013, **1**(37), 11261-11268, DOI 10.1039/c3ta11867c.

38. Rumyantseva, M.N., S.A. Vladimirova, N.A. Vorobyeva, I. Giebelhaus, S. Mathur, A.S. Chizhov, N.O. Khmelevsky, A.Y. Aksenenko, V.F. Kozlovsky, O.M. Karakulina, J. Hadermann, A.M. Abakumov, and A.M. Gaskov, *p-CoO$_x$/n-SnO₂ nanostructures: New highly selective materials for H₂S detection.* Sens. Actuators B, 2018, **255,** 564-571, DOI 10.1016/j.snb.2017.08.096.

39. Shao, F., M.W.G. Hoffmann, J.D. Prades, R. Zamani, J. Arbiol, J.R. Morante, E. Varechkina, M. Rumyantseva, A. Gaskov, I. Giebelhaus, T. Fischer, S. Mathur, and F. Hernández-Ramírez, *Heterostructured p-CuO (nanoparticle)/n-SnO₂ (nanowire) devices for selective H₂S detection.* Sens. Actuators B, 2013, **181,** 130-135, DOI 10.1016/j.snb.2013.01.067.

40. Hackner, A., S. Beer, G. Müller, T. Fischer, and S. Mathur, *Fast responding ephedrine detection with miniaturized surface ionization gas sensors.* Procedia Eng., 2011, **25,** 1325-1328, DOI 10.1016/j.proeng.2011.12.327.

41. Lehnen, T., M. Valldor, D. Nižňanský, and S. Mathur, *Hydrothermally grown porous FeVO₄ nanorods and their integration as active material in gas-sensing devices.* J. Mater. Chem. A, 2014, **2**(6), 1862-1868, DOI 10.1039/c3ta12821k.

42. Ludwig, T., C. Bohr, A. Queraltó, R. Frohnhoven, T. Fischer, and S. Mathur, *Inorganic Nanofibers by Electrospinning Techniques and Their Application in Energy Conversion and Storage Systems*, in *Semiconductors and Semimetals: Nanowires for Energy Applications*, M. Sudha and J. Chennupati, Editors. 2018, Elsevier, p. 1-70, DOI 10.1016/bs.semsem.2018.04.003.

43. von Hagen, R., H. Lorrmann, K.-C. Möller, and S. Mathur, *Electrospun LiFe$_{1-y}$Mn$_y$PO$_4$/C Nanofiber Composites as Self-Supporting Cathodes in Li-Ion Batteries.* Adv. Energy Mater., 2012, **2**(5), 553-559, DOI 10.1002/aenm.201100534.

44. Büyükyazi, M. and S. Mathur, *3D nanoarchitectures of α-LiFeO$_2$ and α-LiFeO$_2$/C nanofibers for high power lithium-ion batteries.* Nano Energy, 2015, **13**(0), 28-35, DOI 10.1016/j.nanoen.2015.02.005.

45. Fei, L., Y. Hu, X. Li, R. Song, L. Sun, H. Huang, H. Gu, H.L. Chan, and Y. Wang, *Electrospun bismuth ferrite nanofibers for potential applications in ferroelectric photovoltaic devices.* ACS Appl. Mater. Interfaces, 2015, **7**(6), 3665-3670, DOI 10.1021/acsami.5b00069.

46. Antony, R.P., P.S. Bassi, F.F. Abdi, S.Y. Chiam, Y. Ren, J. Barber, J.S.C. Loo, and L.H. Wong, *Electrospun Mo-BiVO$_4$ for Efficient Photoelectrochemical Water Oxidation: Direct Evidence of Improved Hole Diffusion Length and Charge separation.* Electrochim. Acta, 2016, **211**, 173-182, DOI 10.1016/j.electacta.2016.06.008.

47. Jamil, A., J. Schläfer, Y. Gönüllü, A. Lepcha, and S. Mathur, *Precursor-Derived Rare Earth Metal Pyrochlores: Nd$_2$Sn$_2$O$_7$ Nanofibers and Thin Films As Efficient Photoabsorbers.* Cryst. Growth Des., 2016, **16**(9), 5260-5267, DOI 10.1021/acs.cgd.6b00815.

48. Lepcha, A., C. Maccato, A. Mettenbörger, T. Andreu, L. Mayrhofer, M. Walter, S. Olthof, T.P. Ruoko, A. Klein, M. Moseler, K. Meerholz, J.R. Morante, D. Barreca, and S. Mathur, *Electrospun Black Titania Nanofibers: Influence of Hydrogen Plasma-Induced Disorder on the Electronic Structure and Photoelectrochemical Performance.* J. Phys. Chem. C, 2015, **119**(33), 18835-18842, DOI 10.1021/acs.jpcc.5b02767.

49. Mathur, S., R. von Hagen, and R. Müller, *One-Dimensional Inorganic Nanomaterials for Energy Storage and Production.* Reference Module in Chemistry, Molecular Sciences and Chemical Engineering. Vol. 4. 2013: Elsevier. 317-341, DOI 10.1016/B978-0-08-097774-4.00414-9.

50.   Queraltó, A. and S. Mathur, *Photoelectrochemical response of Fe₂O₃ films reinforced with BiFeO₃ nanofibers.* MRS Comm., 2018, **8**(03), 1211-1215, DOI 10.1557/mrc.2018.101.

51.   Ding, B. and J. Yu, *Electrospun Nanofibers for Energy and Environmental Applications*. Nanostructure Science and Technology. 2014: Springer Berlin Heidelberg, DOI 10.1007/978-3-642-54160-5.

52.   Choi, S.-H., S.-J. Choi, B.K. Min, W.Y. Lee, J.S. Park, and I.-D. Kim, *Facile Synthesis of p-type Perovskite SrTi₀.₆₅Fe₀.₃₅O₃₋δ Nanofibers Prepared by Electrospinning and Their Oxygen-Sensing Properties.* Macromol. Mater. Eng., 2013, **298**(5), 521-527, DOI 10.1002/mame.201200375.

53.   Cho, N.G. and I.-D. Kim, *NO₂ gas sensing properties of amorphous InGaZnO₄ submicron-tubes prepared by polymeric fiber templating route.* Sens. Actuators B, 2011, **160**(1), 499-504, DOI 10.1016/j.snb.2011.08.017.

54.   Hwang, D.K., S. Kim, J.-H. Lee, I.-S. Hwang, and I.-D. Kim, *Phase evolution of perovskite LaNiO₃ nanofibers for supercapacitor application and p-type gas sensing properties of LaOCl–NiO composite nanofibers.* J. Mater. Chem., 2011, **21**(6), 1959-1965, DOI 10.1039/c0jm02256j.

55.   Nagashima, S., K. Ito, T. Aoki, H. Ishii, and K. Kobayashi. *A High-Accuracy Rotation Estimation Algorithm Based on 1D Phase-Only Correlation*. in *Image Analysis and Recognition*. 2007. Berlin, Heidelberg: Springer Berlin Heidelberg, DOI 10.1007/978-3-540-74260-9_19.

56.   Foroosh, H., J.B. Zerubia, and M. Berthod, *Extension of phase correlation to subpixel registration.* IEEE Trans. Image Process., 2002, **11**(3), 188-200, DOI 10.1109/83.988953.

57.   Takita, K., T. Aoki, Y. Sasaki, T. Higuchi, and K. Kobayashi, *High-Accuracy Subpixel Image Registration Based on Phase-Only Correlation.* IEICE Trans. Fundamentals, 2003. **A86**(8): p. 1925–1934, DOI -.

58.   Yan, H. and J.-G. Liu, *Robust Phase Correlation based Motion Estimation and Its Applications.* The British Machine Vision Conference (BMVC) 2008, 2008, 104.1-104.10, DOI 10.5244/C.22.104.

59.   van Aarle, W., W.J. Palenstijn, J. De Beenhouwer, T. Altantzis, S. Bals, K.J. Batenburg, and J. Sijbers, *The ASTRA Toolbox: A platform for advanced algorithm development in electron tomography.* Ultramicroscopy, 2015, **157,** 35-47, DOI 10.1016/j.ultramic.2015.05.002.

60.   Moon, T.K., *The expectation-maximization algorithm.* IEEE Signal Process. Mag., 1996, **13**(6), 47-60, DOI 10.1109/79.543975.

61.   Klinger, M., *More features, more tools, more CrysTBox.* J. Appl. Crystallogr., 2017, **50**(4), 1226-1234, DOI 10.1107/s1600576717006793.

62.   Patterson, A.L., *The Scherrer Formula for X-Ray Particle Size Determination.* Phys. Rev., 1939, **56**(10), 978-982, DOI 10.1103/PhysRev.56.978.

63.   Qi, W.H. and M.P. Wang, *Size and shape dependent lattice parameters of metallic nanoparticles.* J. Nanoparticle Res., 2005, **7**(1), 51-57, DOI 10.1007/s11051-004-7771-9.

64.   Cazorla, C., *Lattice Effects on the Formation of Oxygen Vacancies in Perovskite Thin Films.* Phys. Rev. Appl., 2017, **7**(4), 044025, DOI 10.1103/PhysRevApplied.7.044025.

65.   Lee, S.A., H. Jeong, S. Woo, J.Y. Hwang, S.Y. Choi, S.D. Kim, M. Choi, S. Roh, H. Yu, J. Hwang, S.W. Kim, and W.S. Choi, *Phase transitions via selective elemental vacancy engineering in complex oxide thin films.* Sci. Rep., 2016, **6,** 23649, DOI 10.1038/srep23649.

66.   Queraltó, A., M. de la Mata, J. Arbiol, R. Hühne, X. Obradors, and T. Puig, *Unveiling the Nucleation and Coarsening Mechanisms of Solution-Derived Self-Assembled Epitaxial $Ce_{0.9}Gd_{0.1}O_{2-y}$ Nanostructures.* Cryst. Growth Des., 2017, **17**(2), 504-516, DOI 10.1021/acs.cgd.6b01358.

67.   Queraltó, A., M. de la Mata, L. Martinez, C. Magen, M. Gibert, J. Arbiol, R. Huhne, X. Obradors, and T. Puig, *Orientation symmetry breaking in self-assembled $Ce_{1-x}Gd_xO_{2-y}$ nanowires derived from chemical solutions.* RSC Adv., 2016, **6**(99), 97226-97236, DOI 10.1039/C6RA23717G.

68.   Rong, Q., Y. Zhang, C. Wang, Z. Zhu, J. Zhang, and Q. Liu, *A high selective methanol gas sensor based on molecular imprinted $Ag-LaFeO_3$ fibers.* Sci. Rep., 2017, **7**(1), 12110, DOI 10.1038/s41598-017-12337-z.

69.   Hoa, N.D., S.Y. An, N.Q. Dung, N. Van Quy, and D. Kim, *Synthesis of p-type semiconducting cupric oxide thin films and their application to hydrogen detection.* Sens. Actuators B, 2010, **146**(1), 239-244, DOI 10.1016/j.snb.2010.02.045.

70.   Lalauze, R., N. Bui, and C. Pijolat, *Interpretation of the electrical properties of a SnO_2 gas sensor after treatment with sulfur dioxide.* Sens. Actuators, 1984, **6**(2), 119-125, DOI 10.1016/0250-6874(84)85005-2.

71.   Das, S., S. Chakraborty, O. Parkash, D. Kumar, S. Bandyopadhyay, S.K. Samudrala, A. Sen, and H.S. Maiti, *Vanadium doped tin dioxide as a novel sulfur dioxide sensor.* Talanta, 2008, **75**(2), 385-389, DOI 10.1016/j.talanta.2007.11.010.

72. Das, S., S. Rana, S.M. Mursalin, P. Rana, and A. Sen, *Sonochemically prepared nanosized BiFeO₃ as novel SO₂ sensor.* Sens. Actuators B, 2015, **218,** 122-127, DOI 10.1016/j.snb.2015.04.084.

73. Várhegyi, E.B., J. Gerblinger, F. Réti, I.V. Perczel, and H. Meixner, *Study of the behaviour of CeO₂ in SO₂-containing environment.* Sens. Actuators B, 1995, **25**(1-3), 631-635, DOI 10.1016/0925-4005(95)85139-9.

74. Vergara, A., S. Vembu, T. Ayhan, M.A. Ryan, M.L. Homer, and R. Huerta, *Chemical gas sensor drift compensation using classifier ensembles.* Sens. Actuators B, 2012, **166-167,** 320-329, DOI 10.1016/j.snb.2012.01.074.

75. Mulmi, S. and V. Thangadurai, *Semiconducting SnO₂-TiO₂ (S-T) composites for detection of SO₂ gas.* Ionics, 2016, **22**(10), 1927-1935, DOI 10.1007/s11581-016-1711-4.

76. Liu, L. and S. Liu, *Oxygen Vacancies as an Efficient Strategy for Promotion of Low Concentration SO₂ Gas Sensing: The Case of Au-Modified SnO₂.* ACS Sust. Chem. Eng., 2018, **6**(10), 13427-13434, DOI 10.1021/acssuschemeng.8b03205.

77. Tyagi, P., A. Sharma, M. Tomar, and V. Gupta, *Efficient Detection of SO₂ Gas Using SnO₂ Based Sensor Loaded with Metal Oxide Catalysts.* Procedia Eng., 2014, **87,** 1075-1078, DOI 10.1016/j.proeng.2014.11.349.

78. Tyagi, P., A. Sharma, M. Tomar, and V. Gupta, *SnO₂ thin film sensor having NiO catalyst for detection of SO₂ gas with improved response characteristics.* Sens. Actuators B, 2017, **248,** 998-1005, DOI 10.1016/j.snb.2017.02.168.

79. Shimizu, Y., N. Matsunaga, T. Hyodo, and M. Egashira, *Improvement of SO₂ sensing properties of WO₃ by noble metal loading.* Sens. Actuators B, 2001, **77**(1-2), 35-40, DOI 10.1016/s0925-4005(01)00669-4.

80. Boudiba, A., C. Zhang, C. Bittencourt, P. Umek, M.-G. Olivier, R. Snyders, and M. Debliquy, *SO₂ Gas Sensors based on WO₃ Nanostructures with Different Morphologies.* Procedia Eng., 2012, **47,** 1033-1036, DOI 10.1016/j.proeng.2012.09.326.

81. Liu, Y., X. Xu, Y. Chen, Y. Zhang, X. Gao, P. Xu, X. Li, J. Fang, and W. Wen, *An integrated micro-chip with Ru/Al₂O₃/ZnO as sensing material for SO₂ detection.* Sens. Actuators B, 2018, **262,** 26-34, DOI 10.1016/j.snb.2018.01.156.

82. Song, Z., Z. Wei, B. Wang, Z. Luo, S. Xu, W. Zhang, H. Yu, M. Li, Z. Huang, J. Zang, F. Yi, and H. Liu, *Sensitive Room-Temperature H₂S Gas Sensors Employing SnO₂ Quantum Wire/Reduced Graphene Oxide Nanocomposites.* Chem. Mater., 2016, **28**(4), 1205-1212, DOI 10.1021/acs.chemmater.5b04850.

83. Milt, V.G., R. Spretz, M.A. Ulla, E.A. Lombardo, and J.L.G. Fierro, *The nature of active sites for the oxidation of methane on La-based perovskites.* Catalysis Lett., 1996, **42**(1-2), 57-63, DOI 10.1007/bf00814467.

84. Zhang, X., G. Dou, Z. Wang, L. Li, Y. Wang, H. Wang, and Z. Hao, *Selective catalytic oxidation of H_2S over iron oxide supported on alumina-intercalated Laponite clay catalysts.* J. Hazard Mater., 2013, **260,** 104-111, DOI 10.1016/j.jhazmat.2013.05.008.

85. Zhu, Y., R. Tan, J. Feng, S. Ji, and L. Cao, *The reaction and poisoning mechanism of SO_2 and perovskite $LaCoO_3$ film model catalysts.* Appl. Catal. A, 2001, **209**(1-2), 71-77, DOI 10.1016/s0926-860x(00)00763-8.

86. Sahner, K., G. Hagen, D. Schonauer, S. Reis, and R. Moos, *Zeolites — Versatile materials for gas sensors.* Solid State Ionics, 2008, **179**(40), 2416-2423, DOI 10.1016/j.ssi.2008.08.012.

87. Xu, J., X. Wang, and J. Shen, *Hydrothermal synthesis of In_2O_3 for detecting H_2S in air.* Sens. Actuators B, 2006, **115**(2), 642-646, DOI 10.1016/j.snb.2005.10.038.

88. Stankova, M., X. Vilanova, E. Llobet, J. Calderer, C. Bittencourt, J.J. Pireaux, and X. Correig, *Influence of the annealing and operating temperatures on the gas-sensing properties of rf sputtered WO_3 thin-film sensors.* Sens. Actuators B, 2005, **105**(2), 271-277, DOI 10.1016/j.snb.2004.06.009.

For Table of Contents Use Only
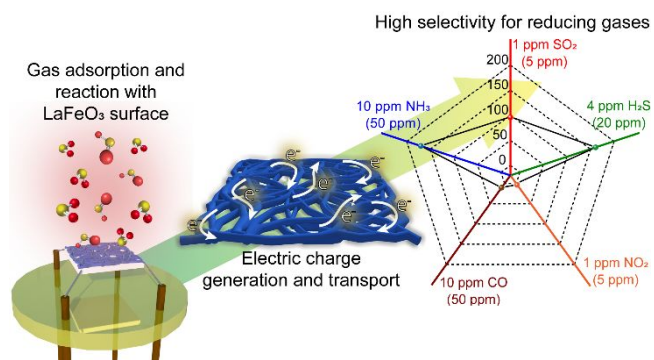
Synopsis: Synthesis of p-type LaFeO$_3$ nanofibers and their extraordinary chemospecificity in detecting sulfur-containing (SO$_2$, H$_2$S) toxic effluents in very small concentrations (0.5-10 ppm) is reported.